SUPPLEMENT TO THE *WELDING JOURNAL*, APRIL 2023
Sponsored by the American Welding Society

Quantitative Interpretation of Dynamic Resistance Signal in Resistance Spot Welding

The evolution mechanism of the dynamic resistance signal in the RSW process was quantitatively revealed using collaborative simulation and analytical modeling

BY Y. J. XIA, T. L. LV, H. GHASSEMI-ARMAKI, Y. B. LI, AND B. E. CARLSON

Abstract

Dynamic resistance is one of the most common and important signals used to monitor and control the resistance spot welding (RSW) process. However, existing studies on the signal evolution mechanism are limited to qualitative analysis, resulting in an ambiguous interpretation of the formation mechanism for the signal features. In this paper, a collaborative simulation approach was applied for the RSW of bare DP590 steel to obtain high-precision computation of the temperature and potential distributions inside the weld. On this basis, an analytical mapping model between the dynamic resistance signal and the weld profile was developed based on basic physical laws, and the signal evolution mechanism was quantitatively revealed through the model. It was found that the main factors determining the signal evolution trend are average sheet temperature and electrode/sheet contact diameter rather than the nugget growth process. The peak resistance feature was attributed to the bilinear relationship between sheet resistivity and temperature rather than nugget formation. The resistance drop after the peak mainly arose from the increase of the electrode/sheet contact diameter rather than nugget growth. This study can help improve the comprehension of the dynamic resistance signal and the interpretability of some data-driven methods used for RSW quality monitoring and control.

Keywords

- Resistance Spot Welding
- Dynamic Resistance Signal
- Evolution Mechanism
- Signal Feature
- Quantitative Interpretation

Introduction

Resistance spot welding (RSW) is a widely used joining method for sheet metal assembly in manufacturing automobiles, railway vehicles, space crafts, etc. A typical steel body-in-white contains nearly 5000 resistance spot welds, and a stainless steel metro car body contains about 20,000 (Ref. 1). According to AWS D8.1M, *Specification for Automotive Weld Quality — Resistance Spot Welding of Steel* (Ref. 2), nugget size is a key indicator for weld quality inspection. However, the nugget is localized between the metal sheets and thus not directly observable. Current quality assessment techniques primarily rely on offline sampling inspection, such as chisel tests and ultrasonic testing. With the rapid increase in the automation rate of welding assembly lines, the shortcomings of these offline sampling inspection approaches in terms of low inefficiency, high cost, and poor reliability are gradually exposed and have become a barrier to the digital transformation of welding plants (Ref. 3). As a result, online monitoring of the transient process signals accompanying the RSW process is a promising method to actualize online weld quality assessment.

Dynamic resistance is one of the most frequently applied process signals (Ref. 4). It can reflect the change in the properties of metal sheets under the combined action of heat and pressure and is considered to be closely related to nugget growth (Ref. 5). Numerous researchers have attempted to develop an online quality inspection method based on the

https://doi.org/10.29391/2023.102.006

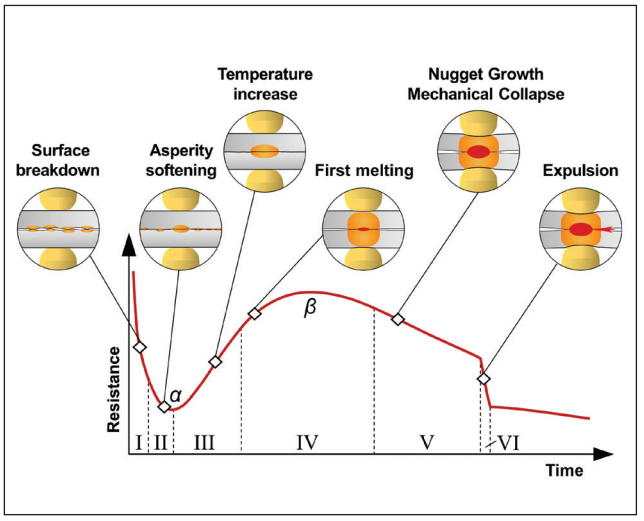

Fig. 1 — Interpretation of the dynamic resistance signal proposed by Dickinson et al. (Ref. 11).

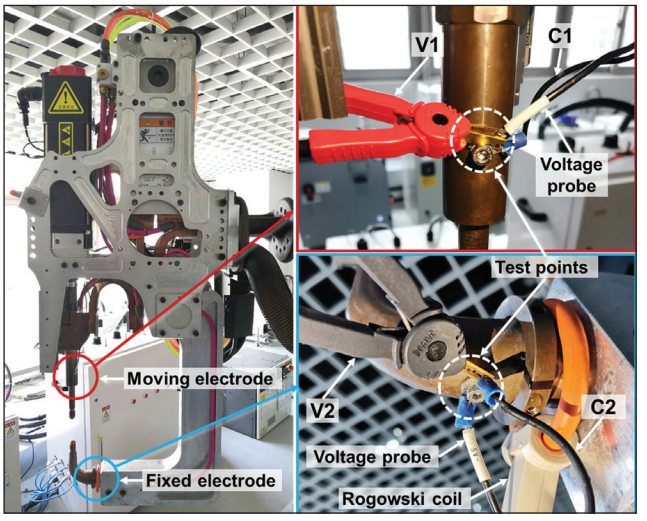

Fig. 2 — Connection diagram for resistance measurement. C1 and C2 are current probes while V1 and V2 are voltage probes for contact resistance measurement.

dynamic resistance signal. The most common practice is to manually extract some time-domain features of the signal waveform (e.g., the peak resistance, the end resistance, the resistance drop after the peak) and then feed them into machine learning models for weld quality prediction. The prediction models could be multiple linear regression (Ref. 6), random forest (Ref. 7), neural network (Refs. 8, 9), etc. Although these approaches have achieved good prediction accuracy in the lab, the correlation mechanism between handcrafted signal features and nugget growth is still unclear. This leads to insufficient interpretability and reduces the reliability of the quality prediction model. Furthermore, the feature extraction lacks a theoretical foundation, making some features less effective than those derived using unsupervised learning (Ref. 10).

To solve these problems, a good explanation of the evolution mechanism of the dynamic resistance signal is required. Currently, the most widely spread interpretation was proposed in 1980 by Dickinson et al. (Ref. 11), who made a qualitative analysis based on experimental results of bare steel and divided the dynamic resistance signal into six stages (I–VI), as shown in Fig. 1. Existing studies (Refs. 12–14) have largely confirmed the soundness of the interpretation of stages I, II, III, and VI. Scholars further studied the effects of different coatings and refined the signal evolution mechanism of stages I–III (e.g., the melting and spreading of the coating would result in multiple local maximum and minimum extremes) (Refs. 15–17). These research studies provide a generalized explanation of the dynamic resistance signal in the early stages from the perspective of the surface contact condition.

However, some disagreements still exist for stages IV and V. The first is the controversial viewpoint that the nugget forms prior to the resistance peak. Luo et al. (Ref. 14) made metallographic observations of welds with different heating durations and found that the first melting (14 ms) preceded the dynamic resistance peak (15 ms). Ighodaro et al. (Ref. 16) and Bag et al. (Ref. 18) performed similar experiments but found that melting started after the peak resistance moment. Secondly, the reason for the resistance drop after its peak is unclear. It should not be caused by the shortening of the current path as a result of mechanical collapse because the distance between two electrodes could keep increasing throughout the heating stage (Ref. 19). According to Wei et al. (Ref. 20), the resistance drop should be due to the decrease in the constriction resistance and the reduction in the growth rate of bulk resistance. This early qualitative interpretation is one-sided and needs to be revised to some extent.

To quantitatively study the dynamic resistance signal, some numerical analysis and modeling methods were employed to obtain some physical information that sensors cannot accurately measure during the RSW process. Cho and Cho (Ref. 21) developed an analytic model via the finite difference method (FDM) to accurately predict the behavior of the dynamic resistance signal as the heat input and electrode force varied. Wang and Wei (Ref. 22) also established a quantitative numerical model using the FDM for the dynamic resistance signal. Based on the model, they divided the dynamic resistance signal into four stages and indicated that nugget formation should lag behind the resistance peak moment. However, the FDM lacks explicit expressions to directly analyze the quantitative correlation between the dynamic resistance signal and nugget size. Recently, Zhou et al. (Ref. 23) developed a comprehensive mathematical model for nugget resistivity measurement based on the physical principle of electrical resistivity. Kas and Das (Ref. 24) proposed a simplified first-order differential equation for dynamic resistance prediction. In these models, the weld section was equated to a circuit model with a mixture of solid metal and liquid metal resistances, and an explicit formula between the weld profile and the dynamic resistance signal was obtained. However, in addition to some physical parameters of the materials, the model required the determination of several unknown parameters whose physical significance was not that clear. Presently, a general model describing the quantitative correlation between the weld geometry and the dynamic resistance signal is not yet available.

Table 1 — Mechanical Properties and Chemical Compositions of DP590

Yield Strength (Mpa)	Tensile Strength (Mpa)	Alloy Elements (wt-%)						
		C	Si	Mn	P	S	Al	Fe
357	527	0.180	0.216	1.643	0.011	0.021	0.037	Bal.

Table 2 — Welding Parameters Applied in the Experiments

Stack-Up Thickness (mm)	Welding Current (kA)	Electrode Force (kN)	Time Period (ms)		
			Squeezing	Heating	Hold
0.8 + 0.8	8	2.6	200	10 ~ 150	200
1.6 + 1.6	8	3.6	200	10 ~ 200	200

This paper proposes a new approach to provide a quantitative interpretation of the dynamic resistance signal, especially for the fourth and fifth stages, as shown in Fig. 1. At first, a collaborative finite element (FE) model that can simultaneously simulate the dynamic resistance signal and the weld profile was established to obtain accurate electric and thermal fields inside the weld. Subsequently, a physics-based analytical model was developed using the simulation's results to reconstruct the dynamic resistance signal. Unlike previous studies, this analytical model does not contain any unexplained pending coefficients. It enables a quantitative analysis of the evolution mechanism of the dynamic resistance signal and reveals the intrinsic reason for the formation of typical signal features.

Research Procedures

Materials and Welding Schedules

The workpiece materials utilized in this study were bare DP590 steel with thicknesses of 0.8 and 1.6 mm. The nominal chemical composition and mechanical properties obtained are provided in Table 1. The original plate was laser cut into sheet coupons that were 130 by 30 mm in size. Two identical sheets were stacked and welded in the center. Welding parameters such as welding current, electrode force, and time schedule were chosen based on General Motors' weld quality standard GMW14057, *Weld Acceptance Criteria and Repair Methods Resistance Spot Welds — Steel*, and are listed in Table 2 (Ref. 25). In addition, the heating time was adjusted around the baseline to conduct a series of welding tests and study the joint development process. The selected heating duration times included 10, 20, 30, 40, 50, 60, 80, 100, 120, 150, and 200 ms.

Experimental Apparatus

Welding experiments were carried out with a WTC 6000s medium-frequency direct-current weld controller and a CenterLine servo gun. The inverter frequency of the power system was 1 kHz, and the cooling water flow rate was 11.3 L/min. Two identical Cu-Zr electrodes (C15000) with tip diameters of 6 mm were employed. Electrode tip dressing was conducted every 15 welds to limit the impact of electrode wear.

Multiple sensors for measuring welding current and secondary voltage were integrated into the servo gun. The current transducer was a Meatrol Rogowski coil with 0.5% accuracy class and was installed on the fixed shank. The voltage probes with shielded twisted pairs were mounted on the upper and lower electrodes — Fig. 2. The output signals of the sensors were collected and averaged every 0.5 ms for further analysis, which is detailed in our previous work (Refs. 26–29). The dynamic resistance signal was calculated according to Ohm's Law:

$$R = \frac{U}{I} - R_b \tag{1}$$

where R is the dynamic resistance signal, U stands for the secondary voltage, I is the welding current, and R_b refers to the base resistance of the electrodes between the two voltage probes, which could be obtained by welding without any workpiece between the electrodes (i.e., the short-circuit test). Moreover, a Hioki RM3548 micro-ohmmeter (0.3% accuracy class) and four probes (V1, V2, C1, and C2) attached to the two electrodes were used to perform the contact resistance test at an output current of 10 A (see Fig. 2). The details are specified in the Contact Property Measurement section.

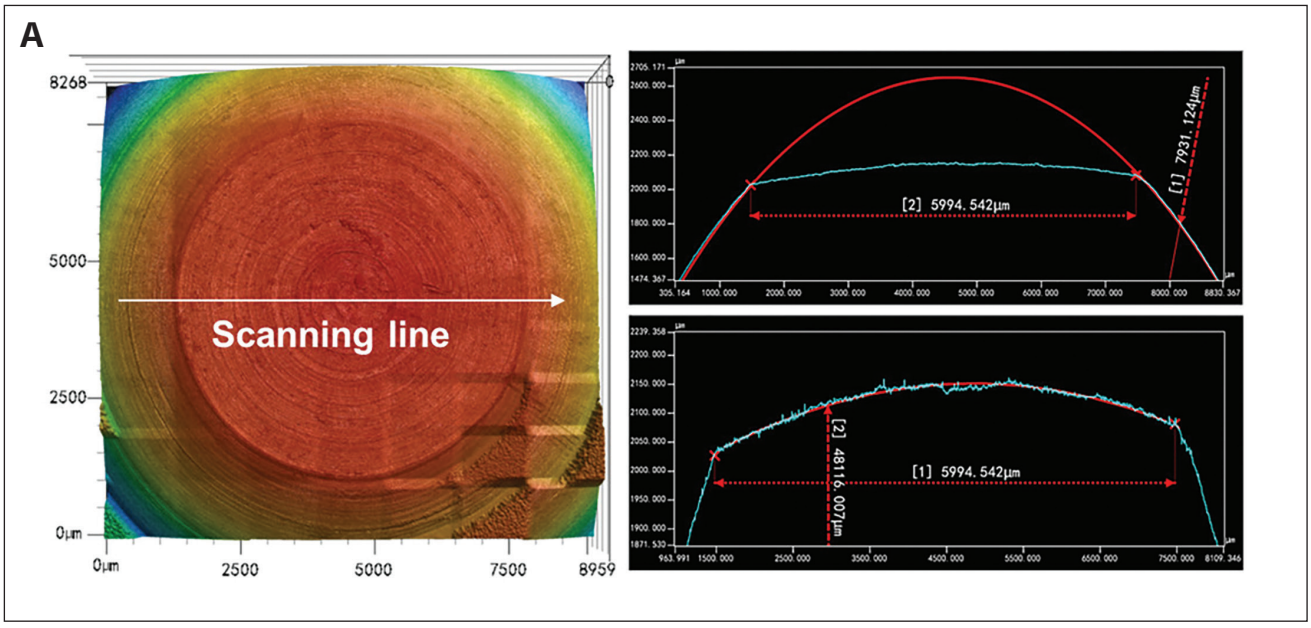

Fig. 3 — Geometric and boundary conditions for the axisymmetric FE model: A — Electrode cap morphology scanned by LCSM; B — dimensions of the electrode cap; C — mechanical boundary conditions; D — thermoelectric boundary conditions.

After welding, the welds were first scanned by a Keyence VK-X200 laser confocal scanning microscope (LCSM) to obtain their surface topography, specifically the indentation diameter. Then the welds were cross sectioned by wire cutting, ground, and polished to a surface finish of 0.05 μm using a Buehler aluminum oxide suspension and, finally, etched with a 4% nital solution. Following the preparation, the nugget profile was examined through a Leica DM2500M metallurgical microscope to distinguish different weld zones, such as the weld nugget, heat-affected zone, and base metal.

Table 3 — Thermophysical Properties of C15000 Copper Alloy (Refs. 31, 32)

Temperature (°C)	Resistivity ($10^{-8}\Omega$m)	Thermal Conductivity (W/(m · K))	Temperature (°C)	Thermal Expansion (10^{-6}/K)	Enthalpy (J/mm³)
20	2.2	326	21	16.6	0
100	2.7	345	93	16.7	0.25
200	3.4	—	204	17.1	0.65
300	4.2	346	316	17.5	1.06
400	4.9	—	427	17.8	1.48
500	5.7	351	538	18.4	1.93
600	6.5	—	649	18.5	2.38
700	7.3	344	760	18.9	2.84
800	8.2	—	871	19.3	—
900	9.1	334	982	19.3	3.77
			1093	—	5.13

Finite Element Modeling

A multiphysics coupled FE model was developed via Ansys 18.0 software. For simplicity, the model only involved thermal (temperature T), electric (potential φ), and mechanical (displacement X) fields. Fluid flow and magnetic effects were ignored. Meanwhile, the electric field within each time step was approximated as quasistatic due to its low changing magnitude. The governing equation included the stress equilibrium, elastic-plastic constitutive, current continuity, and

Table 4 — Thermophysical Properties of DP590 Steel (Refs. 33, 34)

Temperature (°C)	Enpalthy (J/mm^3)	Thermal Expansion ($10^{-6}/K$)	Resistivity ($10^{-8}\Omega m$)	Temperature (°C)	Thermal Conductivity ($W/(m \cdot K)$)
20	0	12.7	28.4	21	46.0
100	0.27	13.0	33.5	109	45.8
200	0.66	13.7	40.2	306	42.7
300	1.09	14.3	47.8	496	37.5
400	1.55	15.2	56.4	600	34.4
500	2.06	15.5	66.6	692	30.7
600	2.62	15.6	80.6	796	26.7
800	4.06	12.7	114.0	1196	30.0
1000	5.10	13.8	121.2	1400	33.1
1200	5.98	15.8	124.9	1504	35.0
1500	7.36	17.7	134.1	1520	36.5
1520	8.99	27.8	140.3	2400	42.5
2000	11.0	32.3	144.5		

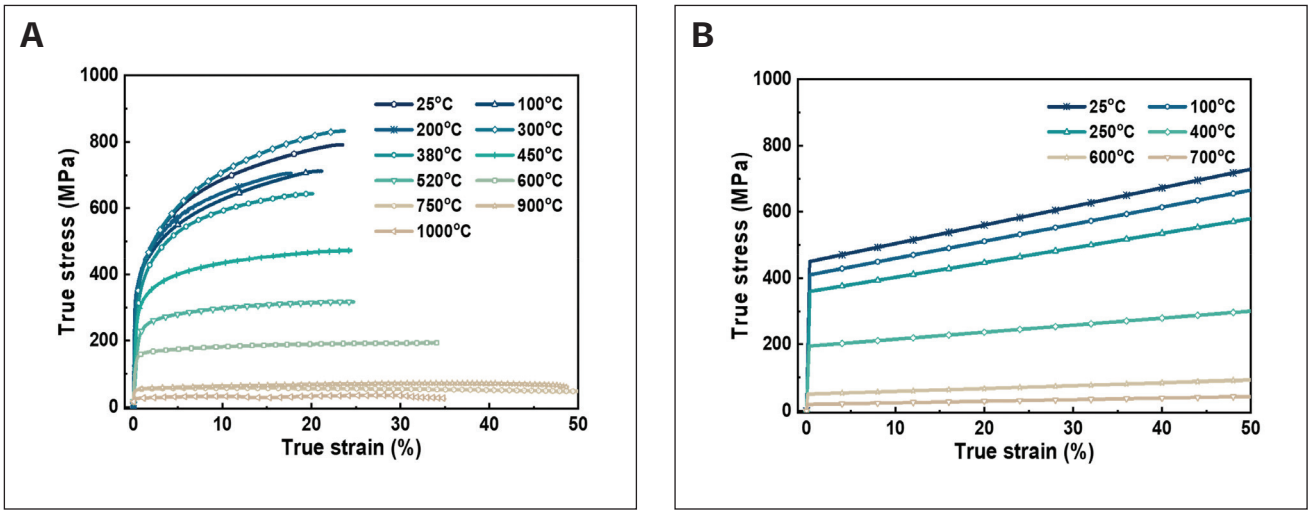

Fig. 4 — Temperature-dependent true stress-strain curves for applied materials: A — DP590 steel; B — C15000 copper alloy.

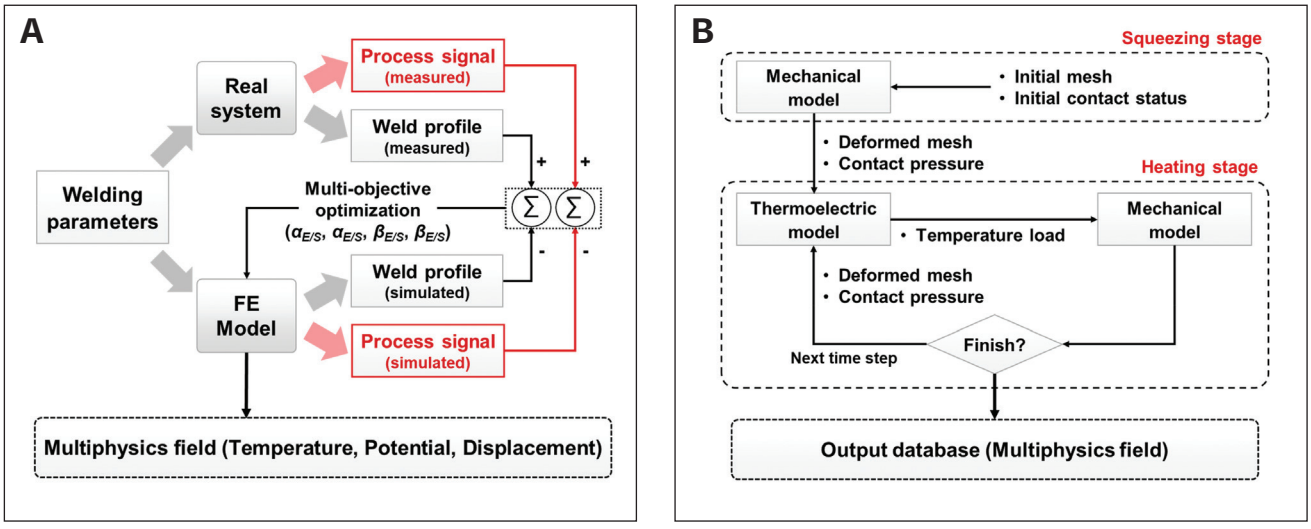

Fig. 5 — Collaborative simulation strategy for the RSW process: A — Optimization strategy; B — solution procedure.

heat conduction equations, whose specific expressions could be found in previous studies (Refs. 30, 31).

Figure 3 depicts the simplified 2D axisymmetric geometric model for the RSW system consisting of two domed electrode caps and two layers of sheets. The tip face diameter of the electrode was set as 6 mm and the radius of curvature of the tip was 50 mm, which were obtained from the LCSM, as shown in Fig. 3A. The mesh in the contact area between the sheets and electrode caps was locally refined with a minimum mesh size of 20 × 20 μm, while the mesh in the other areas was sparse. The mechanical and thermoelectric boundary conditions are shown in Figs. 3C and D, respectively. A fixed constraint was applied at the bottom of the lower electrode cap, and the electric potential and axial displacement were forced to zero. The electrode force and welding current were uniformly distributed on the top of the upper electrode cap. Additionally, in the thermal field, the room temperature T_0 was set as 20°C. The notations q' and q'' denote the surface heat flux density for convection with atmosphere and cooling water, respectively. The convective heat transfer coefficients of air (h_a) and cooling water (h_w) were assumed to be 19.4 W/(m²K) and 3800 W/(m²K), respectively (Ref. 31).

Tables 3 and 4 list the temperature-dependent material properties of the C15000 copper alloy and DP590 steel, respectively, including electrical resistivity, thermal conductivity, thermal expansion coefficient, and enthalpy (Refs. 31–34). The temperature-dependent mechanical properties were modeled with the von Mises yield criterion using a multilinear isotropic hardening model for the steel sheet and a bilinear isotropic hardening model for the Cu-Zr electrode. The stress-strain curves for the C15000 copper alloy were from published literature (Ref. 27), while the curves for the DP590 steel were obtained from high-temperature tensile tests using a Zwick Z100 testing machine with a tensile loading rate of 0.001/s — Fig. 4.

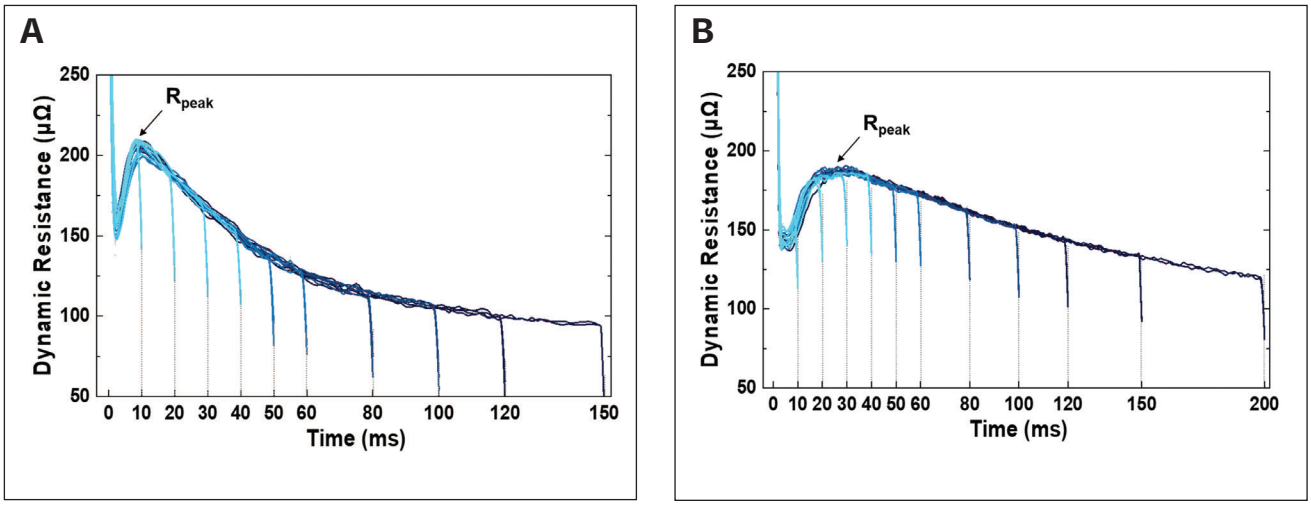

Fig. 6 — Experimental data of dynamic resistance signals for different sheet stack-ups: A — 0.8 + 0.8-mm DP590; B — 1.6 + 1.6-mm DP590.

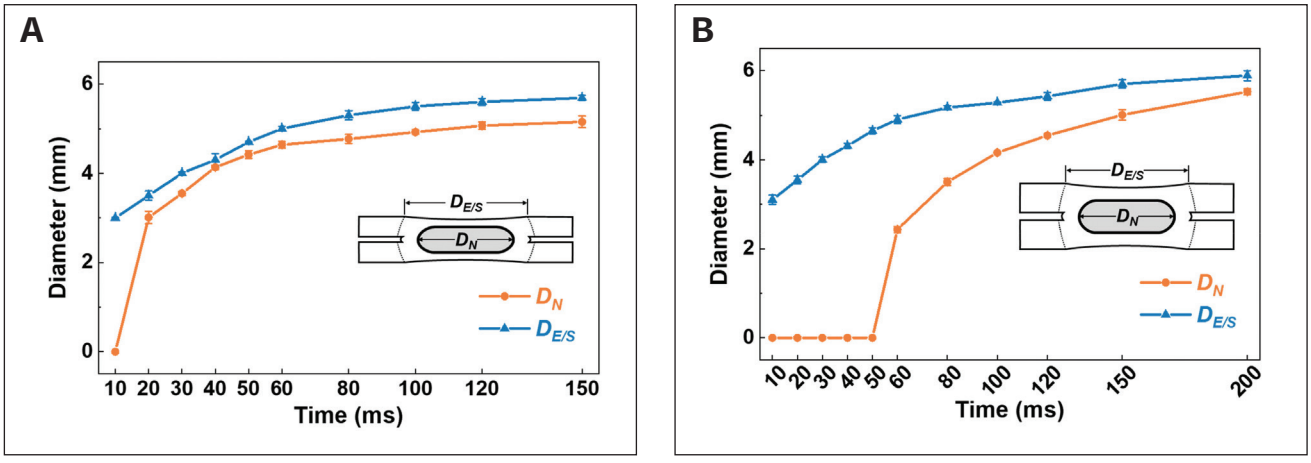

Fig. 7 — Experimental data of both nugget and indentation diameters for different sheet stack-ups: A — 0.8 + 0.8-mm DP590; B — 1.6 + 1.6-mm DP590.

Furthermore, a well-performing contact model developed by the commercial simulation software SORPAS® (Ref. 35) and modified by Wan et al. (Ref. 31) was employed to represent the electrical and thermal contact properties of the contact pairs in Fig. 3C:

$$\begin{cases} ECR_{A/B}(T,P) = \alpha_{A/B} \cdot ECR_{A/B}(T_0,P)\left(\frac{\sigma_{s\text{-}A/B}(T)}{\sigma_{s\text{-}A/B}(T_0)}\right)^{K_C}\left(\frac{\rho_A(T)+\rho_B(T)}{\rho_A(T_0)+\rho_B(T_0)}\right) \\ TCR_{A/B}(T,P) = \beta_{A/B} \cdot \frac{ECR_{A/B}(T,P)}{L_C T} \end{cases} \quad (2)$$

where $ECR_{A/B}(T, P)$ and $TCR_{A/B}(T, P)$ are the electrical contact resistance (ECR) and thermal contact resistance (TCR) of the A/B interface at temperature T and pressure P, respectively. $\alpha_{A/B}$ and $\beta_{A/B}$ are the adjustable correction coefficients to be optimized. $\sigma_{s\text{-}A/B}(T)$ stands for the yield strength of the softer of materials A and B at temperature T. $\rho_A(T)$ and $\rho_B(T)$ are the resistivities of materials A and B at temperature T, respectively. The factor K_C is related to the oxide layer or coating layer on the material surface and varies from 1.0 to 1.5. In this study, K_C was set as 1.0 because the sheet surface was bare and clean. L_C denotes the Lorentz constant, whose value is 2.44×10^{-8} WΩ/K². In the RSW system, the A/B interface should be one of the electrode/sheet (E/S) and sheet/sheet (S/S) interfaces.

Collaborative Simulation Strategy

Figure 5B gives the coupling procedure for the simulation of the RSW process. For ease of solution convergence, a mechanical model independent of a thermoelectric model with the identical FE meshes depicted in Fig. 3 was established. The time step was set as 0.5 ms. In each time step, the thermoelectric and structural fields were solved in turn. The temperature load output from the thermoelectric field served as an initial condition of the structural field, while the mesh and contact pressure outputs from the structural field were transferred to the thermoelectric field to update the ECR and TCR.

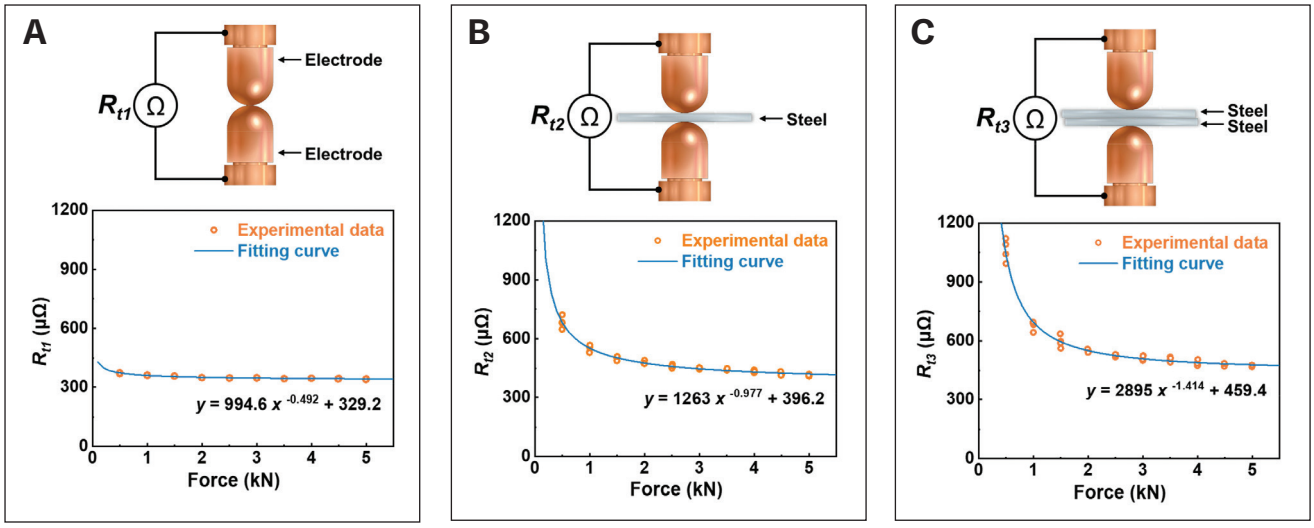

Fig. 8 — Resistance measurements under different conditions: A — No sheet; B — single-layer sheet; C — double-layer sheet.

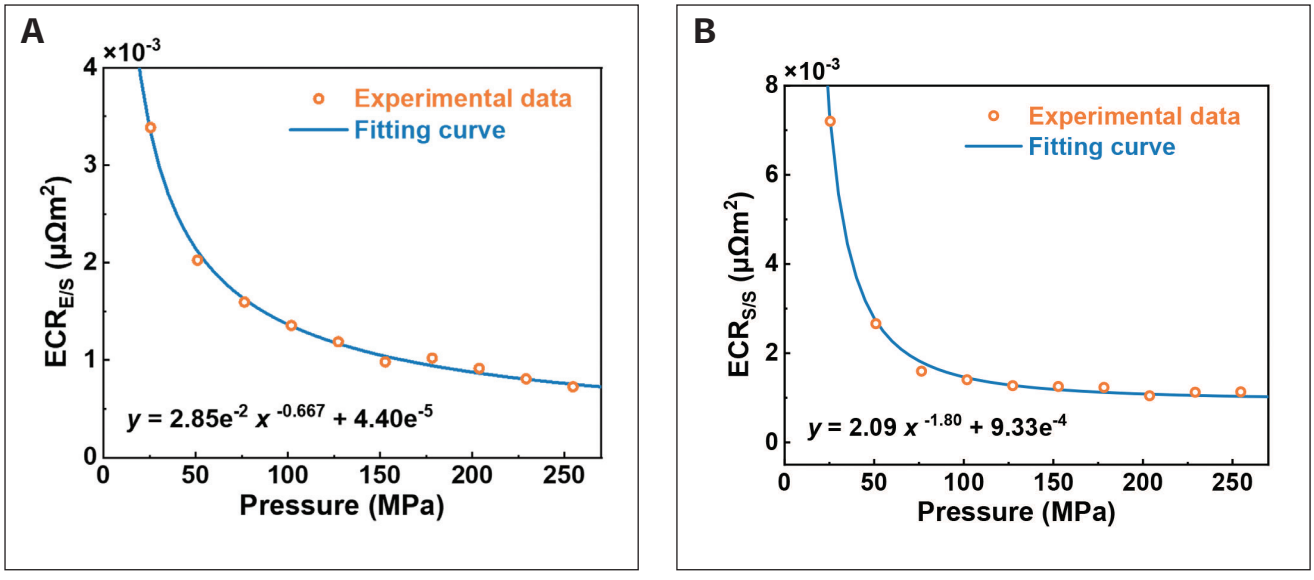

Fig. 9 — Electrical contact resistance as a function of pressure at room temperature for different interfaces: A — E/S interface; B — S/S interface.

In the aforementioned FE model, the development of contact models for the E/S and S/S interfaces involved the measurement of $ECR_{E/S}(T_0, P)$ and $ECR_{S/S}(T_0, P)$ and the determination of four adjustable coefficients, including $\alpha_{E/S}$, $\alpha_{S/S}$, $\beta_{E/S}$, and $\beta_{S/S}$. The former is specified in the Contact Property Measurement section. Figure 5A shows the collaborative optimization strategy for the four adjustable coefficients. Unlike previous studies, not only weld profiles (namely nugget diameter and indentation diameter) but also process signals (including dynamic resistance) were simulated and compared with the measured ones to achieve a multiobjective optimization of the undetermined coefficients. This collaborative approach was inspired by the simple idea that the simulated weld geometry mainly verified the temperature distribution, while verifying the potential and displacement distributions required dynamic resistance and electrode displacement signals.

Results

Resistance Signal and Weld Profile

Figure 6 demonstrates the measured dynamic resistance signals in the welding test with various heating times listed in Table 2. It should be emphasized that the sheets used in this work were uncoated. For each duration time, more than three replicas were made. As shown, the signals of all welds followed a similar pattern, implying the tests were consistent. It was discovered that the dynamic resistance signal R exhibited an evolution trend similar to that shown in Fig. 1.

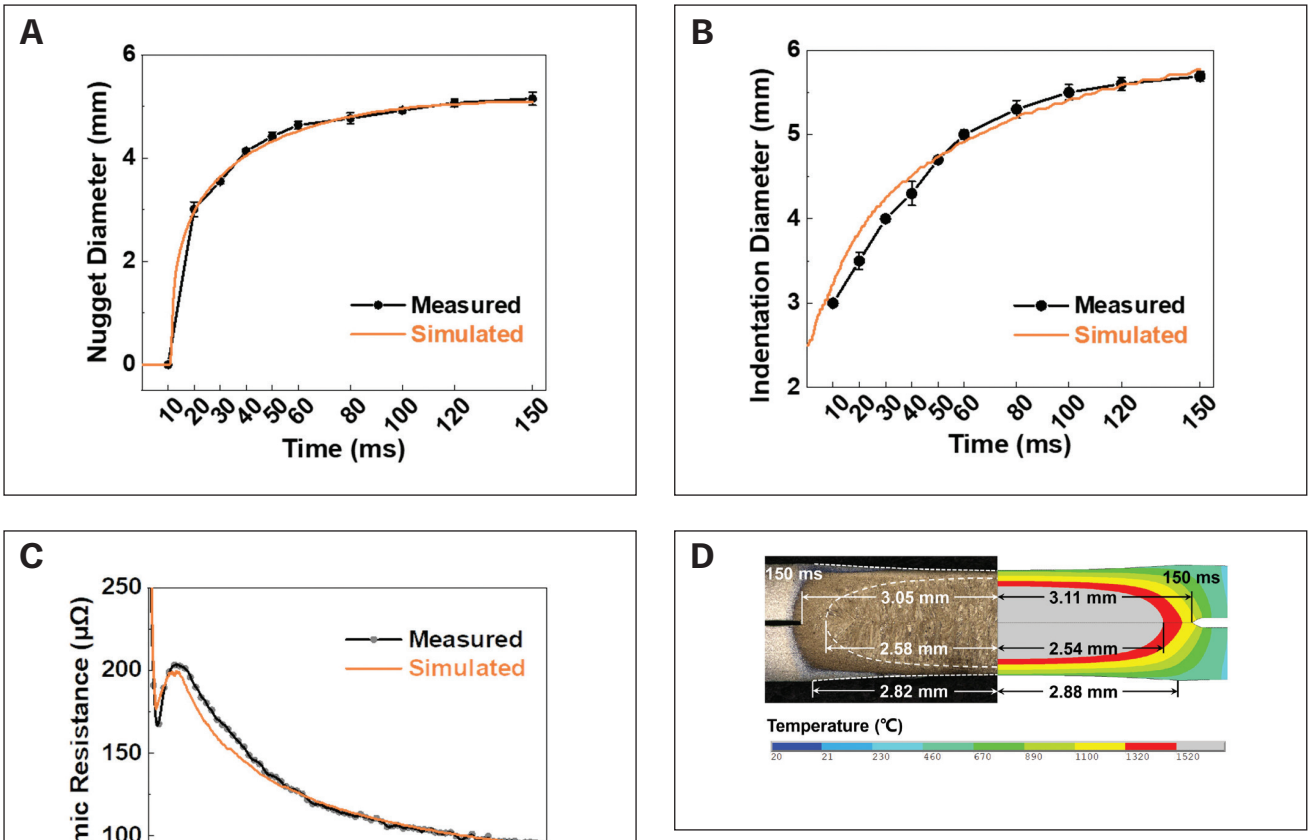

Fig. 10 — Comparison between the simulated and measured results for 0.8 + 0.8-mm DP590 sheet welding tests: A — Nugget diameter; B — indentation diameter; C — dynamic resistance; D — cross-section profile.

The resistance peak (R_{peak}) arose at approximately 10 ms for 0.8 + 0.8-mm sheet stack-up and around 30 ms for 1.6 + 1.6-mm sheet stack-up.

Figure 7 shows the measured weld profile in the welding tests with different heating times. Each datum was derived from the average of more than three replicas. Because of the good consistency of the process signals, this could be regarded as the growth of the weld nugget and surface indention during a single welding process. The measured indentation diameter at different welding times could be regarded as the dynamic E/S contact diameter. As shown, both the nugget diameter (D_N) and the indentation diameter ($D_{E/S}$) grew with increasing heating time. For 0.8 + 0.8-mm sheet stack-up, the moment of nugget formation should be between 10 and 20 ms. But for the 1.6 + 1.6-mm sheet stack-up, the moment was between 50 and 60 ms.

Contact Property Measurement

The measurement of $ECR_{E/S}(T_0, P)$ and $ECR_{S/S}(T_0, P)$ in Equation 2 was carried out in two steps. Firstly, the servo gun was closed at different electrode forces (0.5 ~ 5 kN) to test the total resistance under the following three conditions: with no sheet, single sheet, and double sheets. Three replicate measurements were performed at each force. The measurements were recorded as R_{t1}, R_{t2}, and R_{t3}, correspondingly, as shown in Fig. 8. It can be seen that the resistance measurements for the three conditions decreased with the increasing force. This was mainly caused by the reduction of the interface resistance. Furthermore, three exponential functions were chosen to fit the relationship between resistance and force.

Secondly, the resistance measurements were expressed as follows using the equivalent series circuit model:

$$\begin{cases} R_{t1} = R_{\mathrm{C/E}} + 2R_E + R_{\mathrm{E/E}} \\ R_{t2} = R_{\mathrm{C/E}} + 2R_E + 2R_{\mathrm{E/S}} + R_S \\ R_{t3} = R_{\mathrm{C/E}} + 2R_E + 2R_{\mathrm{E/S}} + 2R_S + R_{\mathrm{S/S}} \end{cases} \quad (3)$$

where $R_{C/E}$, $R_{E/E}$, $R_{E/S}$, and $R_{S/S}$ are resistances of probe/electrode, electrode/electrode, E/S, and S/S interfaces. R_S and R_E represent the bulk resistances of one electrode and one sheet, respectively. Assuming that $R_{E/E}$ is the negligible force reaching infinity, then

$$R_{t1}^{\infty} = \lim_{F \to \infty} R_{t1} = R_{\mathrm{C/E}} + 2R_E \quad (4)$$

where R_{t1}^{∞} is the limit in mathematics of the fitting func-

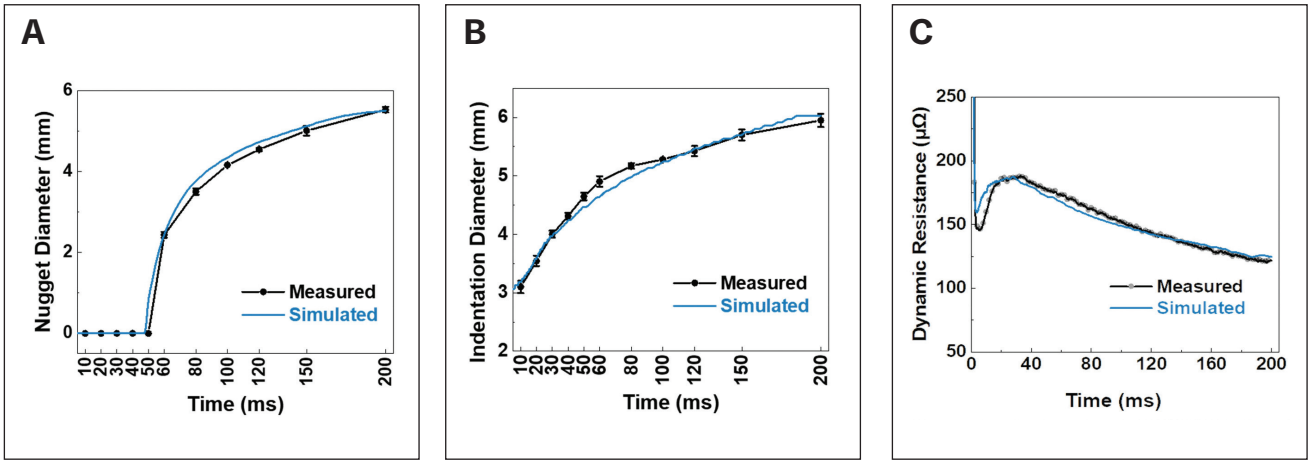

Fig. 11 — Comparison between the simulated and measured results for 1.6 + 1.6-mm DP590 sheet welding tests: A — Nugget diameter; B — indentation diameter; C — dynamic resistance.

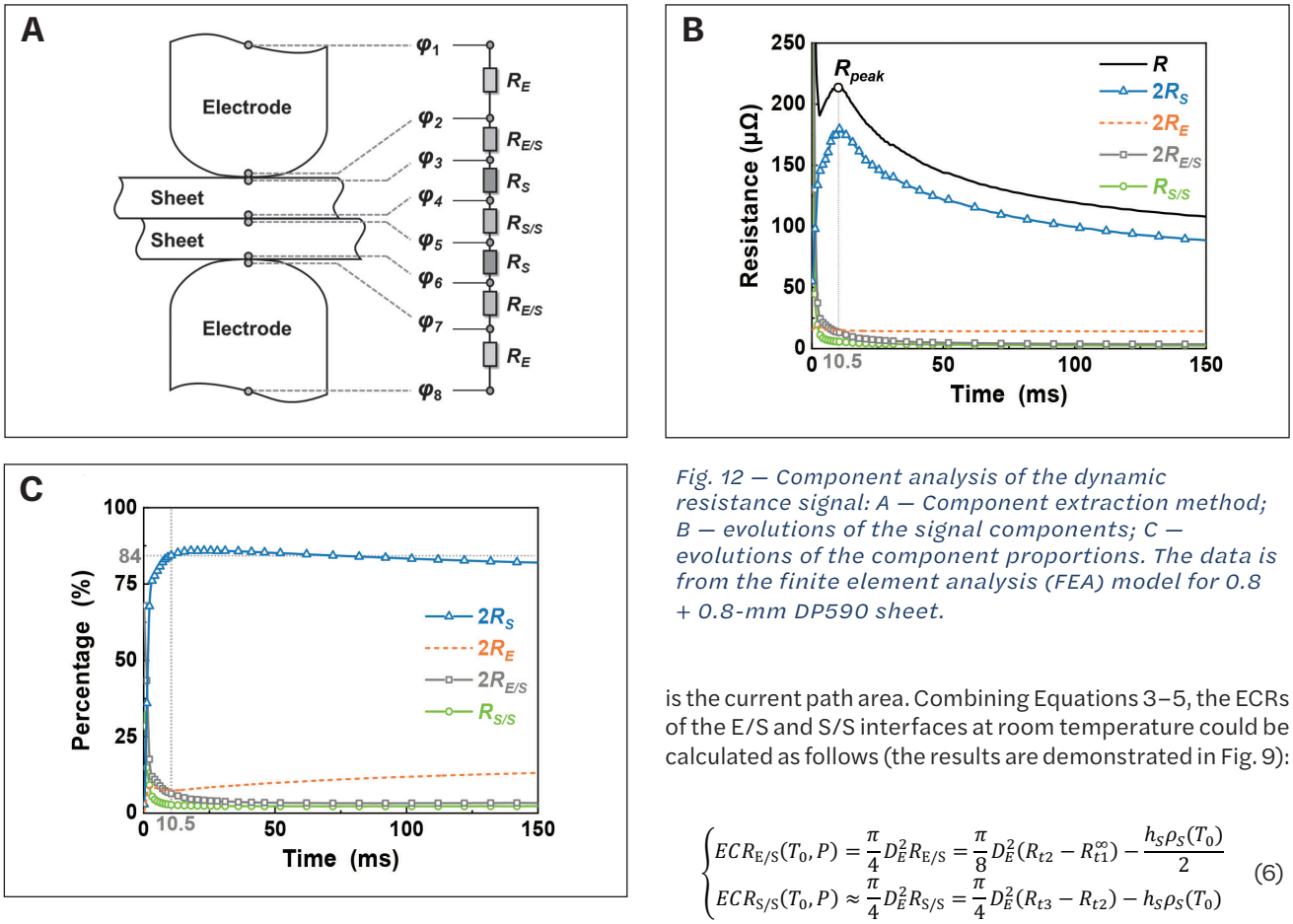

Fig. 12 — Component analysis of the dynamic resistance signal: A — Component extraction method; B — evolutions of the signal components; C — evolutions of the component proportions. The data is from the finite element analysis (FEA) model for 0.8 + 0.8-mm DP590 sheet.

tion, which equals 329.2 μΩ. Moreover, R_S can be calculated according to the Law of Resistance:

$$R_S = \rho_S(T_0)\frac{h_S}{A_{CP}} \approx \frac{4h_S\rho_S(T_0)}{\pi D_{E/S}^2} \quad (5)$$

where $\rho_S(T_0)$ stands for the resistivity of the sheet at room temperature (see Table 4), h_S is the sheet thickness, and A_{CP} is the current path area. Combining Equations 3–5, the ECRs of the E/S and S/S interfaces at room temperature could be calculated as follows (the results are demonstrated in Fig. 9):

$$\begin{cases} ECR_{E/S}(T_0,P) = \frac{\pi}{4}D_E^2R_{E/S} = \frac{\pi}{8}D_E^2(R_{t2} - R_{t1}^{\infty}) - \frac{h_S\rho_S(T_0)}{2} \\ ECR_{S/S}(T_0,P) \approx \frac{\pi}{4}D_E^2R_{S/S} = \frac{\pi}{4}D_E^2(R_{t3} - R_{t2}) - h_S\rho_S(T_0) \end{cases} \quad (6)$$

Validation of Simulated Results

According to the simulation strategy shown in Fig. 5A, a full factorial experimental design was used to optimize the four undetermined correction coefficients, and the range of parameters was set as 0.01 ~ 10. The ultimately modified

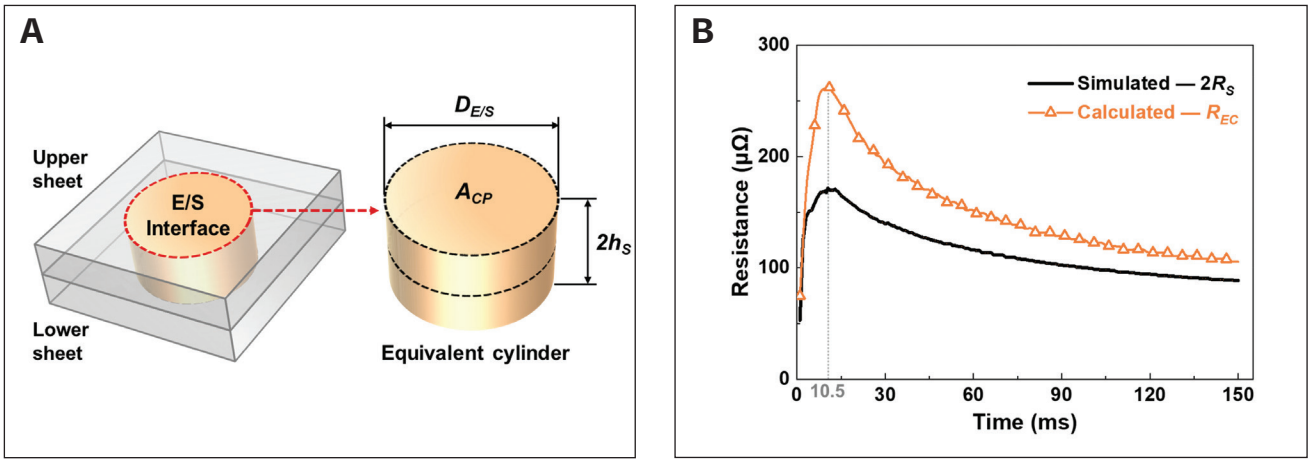

Fig. 13 — Analytical mapping modeling of the sheet resistance component: A — The equivalent cylinder assumption; B — comparison of estimated and simulated sheet resistances. The data is from the FEA model for 0.8 + 0.8-mm DP590 sheet.

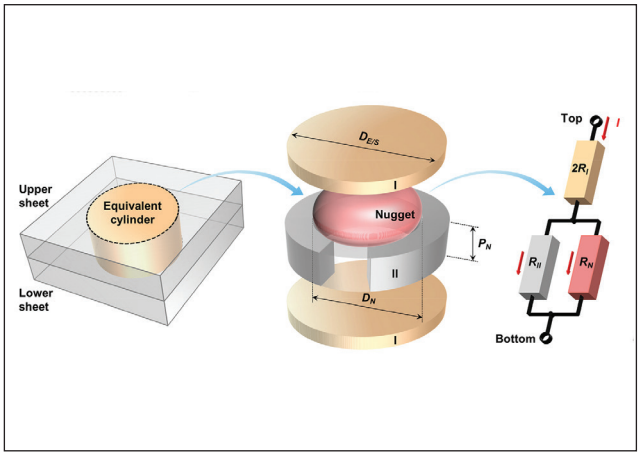

Fig. 14 — Schematic diagram of the equivalent circuit model of sheet resistance.

parameters were $\alpha_{E/S} = 2.8$, $\alpha_{S/S} = 0.33$, $\beta_{E/S} = 0.36$, and $\beta_{S/S} = 1.0$. The simulated results of the radial weld profile and dynamic resistance signal are displayed in Fig. 10. The simulated dynamic resistance signal was obtained by dividing the potential at the top of the upper electrode by the welding current and then subtracting the bulk resistance of the electrodes. As shown, the optimized FE model achieved simultaneous precision simulation of the nugget diameter, indentation diameter, and dynamic resistance signal and provides an accurate simulation of the peak feature of the dynamic resistance signal.

In addition, the developed FE model can adapt to the sheet thickness variation. Figure 11 shows the simulated results for 1.6 + 1.6-mm sheet stack-up with the same modified parameters. The simulated nugget evolution and dynamic resistance signal are highly coincident with the actual measurements, which at least indicates that the FE model simulations are accurate for both the temperature and potential distributions. In fact, the model also enables a high precision simulation of the axial weld profile and electrode displacement signal. The results will be made public in the future.

Discussion

Signal Component Analysis

In the verified FE model, the RSW system can be approximated as an equivalent circuit connected by a series of resistance components, including sheet resistance R_S, electrode resistance R_E, and contact resistances $R_{E/S}$ and $R_{S/S}$, as shown in Fig. 12A. All the components are time varying and can be obtained from the potentials φ_i ($i = 1 \sim 8$) of some key nodes (Ref. 22). Under the symmetric condition, the overall dynamic resistance signal R can be expressed using the equivalent series circuit model as follows:

$$R = 2R_S + 2R_E + 2R_{E/S} + R_{S/S} \quad (7)$$

The evolution of each dynamic resistance component is depicted in Fig. 12B. At the beginning of the heating stage, $R_{E/S}$ and $R_{S/S}$ declined rapidly due to the combined effect of heat and pressure, resulting in a sharp decrease in R. On the contrary, R_S rose fast at the beginning, peaked around 10.5 ms, and then steadily dropped as weld time increased. Due to the decrease of contact resistances, the proportion of R_S to R climbed rapidly and reached roughly 84% after 10.5 ms, making the subsequent trajectory of R essentially consistent with R_S. Additionally, R_E remained around 14 μΩ throughout the heating stage and showed a minor effect. As a result, in this system with bare steel sheets, R_S was the most critical component determining the evolution trend of R, especially during stages III–V depicted in Fig. 1. In the subsequent sections, the analysis focuses on sheet resistance R_S.

Quantitative Mapping Modeling

According to the Law of Resistance, R_S is related to sheet resistivity, sheet thickness, and current path area, assuming that current lines are distributed inside a cylinder with a bottom area of A_{CP} and a height of $2h_S$, which is named

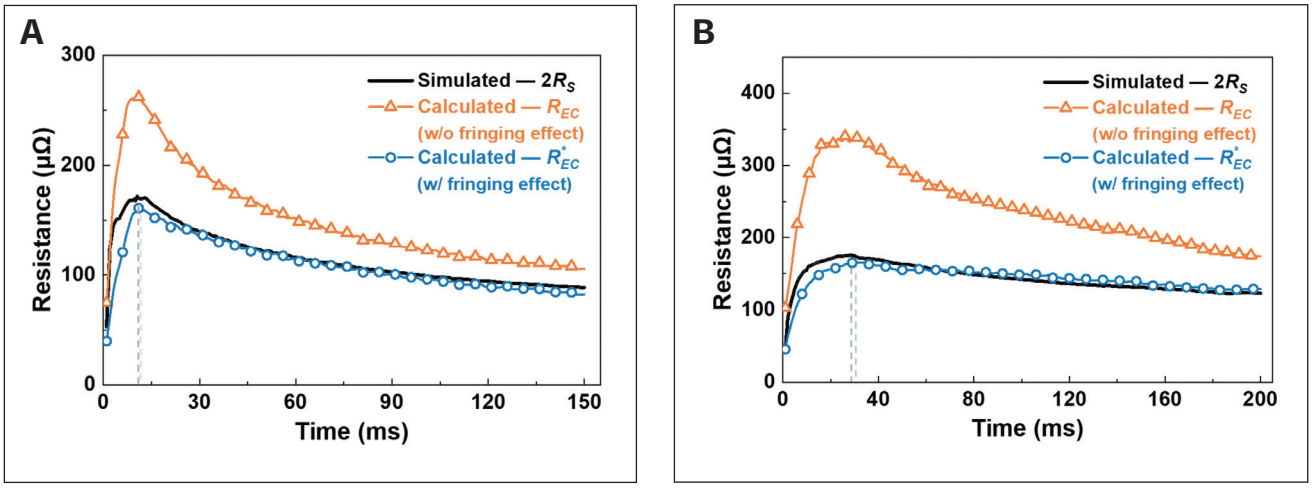

Fig. 15 — Comparison of estimated and simulated results of sheet resistance for different sheet stack-ups: A — 0.8 + 0.8-mm DP590; B — 1.6 + 1.6-mm DP590.

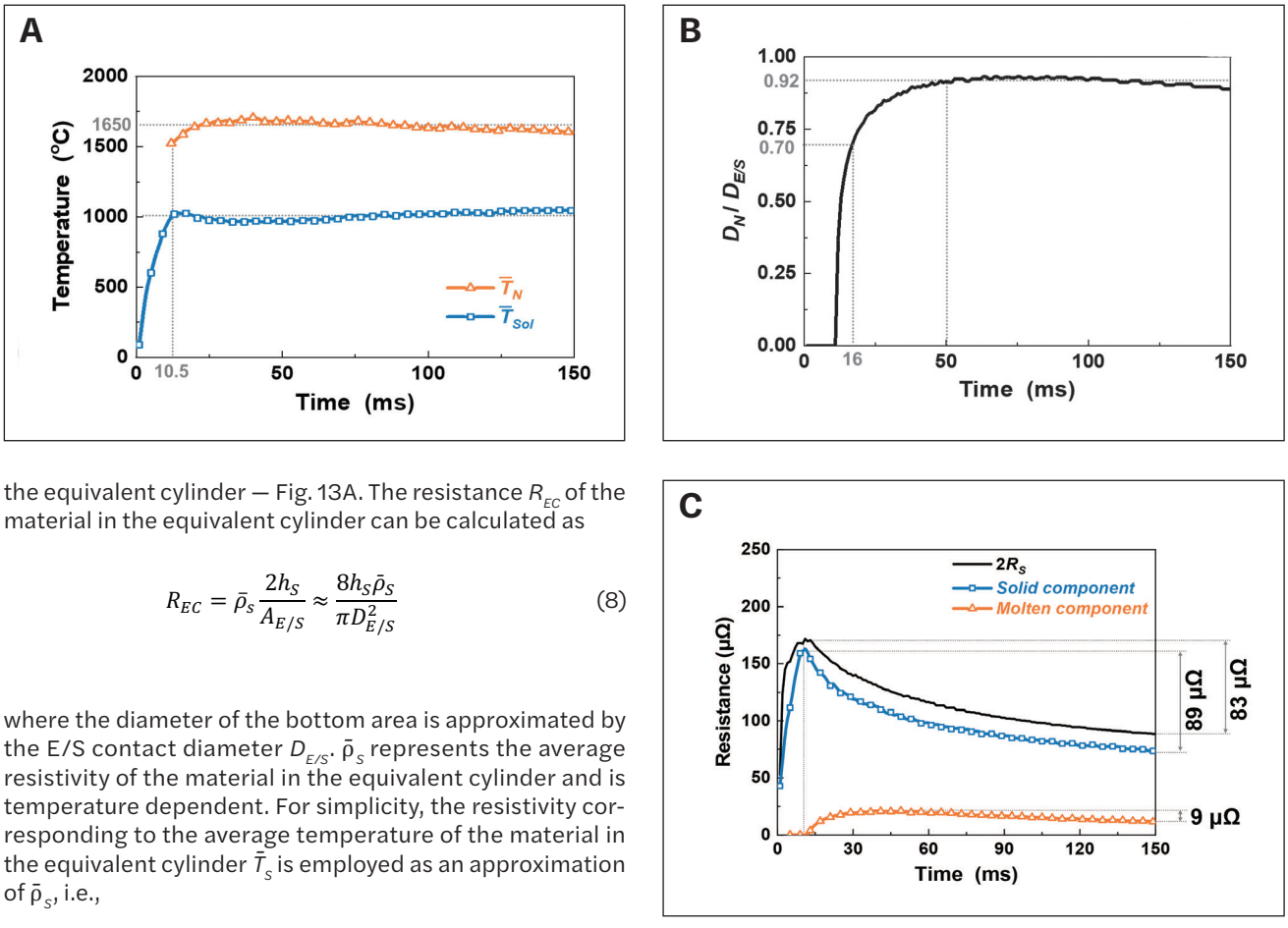

Fig. 16 — Evolution mechanism analysis of the dynamic resistance signal: A — Evolution of the average sheet temperature; B — evolution of the ratio of nugget diameter and indentation diameter; C — evolution of different signal components. The data is from the FEA model for 0.8 + 0.8-mm DP590 sheet.

the equivalent cylinder — Fig. 13A. The resistance R_{EC} of the material in the equivalent cylinder can be calculated as

$$R_{EC} = \bar{\rho}_S \frac{2h_S}{A_{E/S}} \approx \frac{8h_S\bar{\rho}_S}{\pi D_{E/S}^2} \tag{8}$$

where the diameter of the bottom area is approximated by the E/S contact diameter $D_{E/S}$. $\bar{\rho}_S$ represents the average resistivity of the material in the equivalent cylinder and is temperature dependent. For simplicity, the resistivity corresponding to the average temperature of the material in the equivalent cylinder $\bar{T}_S$ is employed as an approximation of $\bar{\rho}_S$, i.e.,

$$\bar{\rho}_S \approx \rho_S(\bar{T}_S) \tag{9}$$

Therefore, only two time-varying input variables are required to analytically calculate R_{EC}: the average sheet temperature $\bar{T}_S$ and the E/S contact diameter $D_{E/S}$, wherein $\bar{T}_S$ can be obtained by integrating the temperature data of the

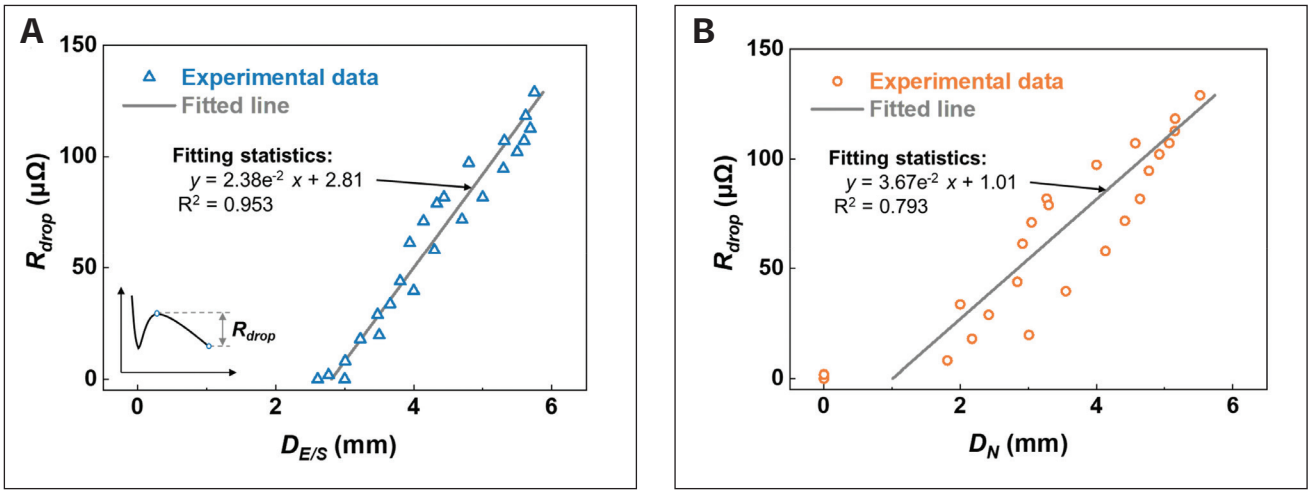

Fig. 17 — Relationship between the resistance drop feature and different weld profiles for 0.8 + 0.8-mm DP590 sheet welding tests: A — Indentation diameter vs. resistance drop feature; B — nugget diameter vs. resistance drop feature.

elements inside the equivalent cylinder from the FE model. Figure 13B gives the comparison between the calculated R_{EC} and the simulated R_S. It can be seen that both the calculated and simulated results showed a firstly increasing and then decreasing trend with the peak occurring at around 10.5 ms. However, the calculated R_{EC} was significantly larger than the simulated R_S. The disparity primarily arose from the inappropriate assumption of the current conduction path (i.e., the neglect of the fringing effect). On the one hand, the radial section area of the sheet was much larger than the E/S contact area. On the other hand, current selects the path of least resistance and prefers to be distributed in the external low-temperature region. As a result, the actual current conduction region in the sheets was much larger than the volume of the equivalent cylinder, resulting in R_S being smaller than R_{EC}.

Some modifications should be made to Equation 8 to consider the fringing effect. According to the analogy between a constant electric field and an electrostatic field, the current distribution in a conductive medium can be equated to the potential distribution in a dielectric. Thus, under the quasistatic electric field assumption, the sheet conductance (the reciprocal of the sheet resistance) between two circular electrode tips can be analogous to the capacitance of a parallel disk capacitor with the same dimensions. To take into account the fringing effect, the capacitance of a parallel disk capacitor should be modified by multiplying a correction factor ω_f, which can be approximated through the formula proposed by Kirchhoff (Ref. 36) as follows:

$$\begin{cases} \omega_f = 1 + \dfrac{W}{\pi} ln\left(\dfrac{16\pi}{W} - 1\right) \\ W = \dfrac{2h_S}{D_{E/S}} \end{cases} \tag{10}$$

where W stands for the aspect ratio. In the double-layer sheet system, W should equal the ratio of the total sheet thickness and the E/S contact diameter. Therefore, according to the electrostatic analogy, the sheet resistance value can also be corrected by dividing itself with this factor.

Meanwhile, the equivalent cylinder was divided into three zones: zone I, zone II, and the fusion zone (weld nugget) to deal with the difference in resistivity existing between solid and molten regions of the sheets, as shown in Fig. 14. With these corrections, the modified resistance R_{EC}* of the equivalent cylinder was directly obtained using the equivalent mixed circuit model:

$$R_{EC}^{*} = \frac{2R_I + R_{II} \parallel R_N}{\omega_f} = \frac{2R_I}{\omega_f} + \frac{R_{II}R_N}{\omega_f(R_{II} + R_N)} \tag{11}$$

where R_I, R_{II}, and R_N denote the resistances of zone I, zone II, and the weld nugget, respectively. According to the Law of Resistance, the resistances of these three regions are

$$\begin{cases} R_I \approx \dfrac{4}{\pi}\rho_S(\bar{T}_{Sol})\dfrac{h_S - \dfrac{P_N}{2}}{D_{E/S}^2} \\ R_{II} \approx \dfrac{4}{\pi}\rho_S(\bar{T}_{Sol})\dfrac{P_N}{D_{E/S}^2 - D_N^2} \\ R_N \approx \dfrac{4}{\pi}\rho_S(\bar{T}_N)\dfrac{P_N}{D_N^2} \end{cases} \tag{12}$$

where P_N is the nugget thickness. $\bar{T}_{Sol}$ and $\bar{T}_N$ represent the average temperature of the solid and molten regions in the sheets, respectively. They can be obtained from the FE model similarly to $\bar{T}_S$.

Figure 15 compares the calculated R_{EC}* and simulated R_S. It was found that the calculated R_{EC}* matched the simulated sheet resistance more closely due to the correction for the fringing effect, especially the part after the resistance peak. The disparity before the resistance peak mainly arose from the nonlinear relationship between the sheet resistivity and

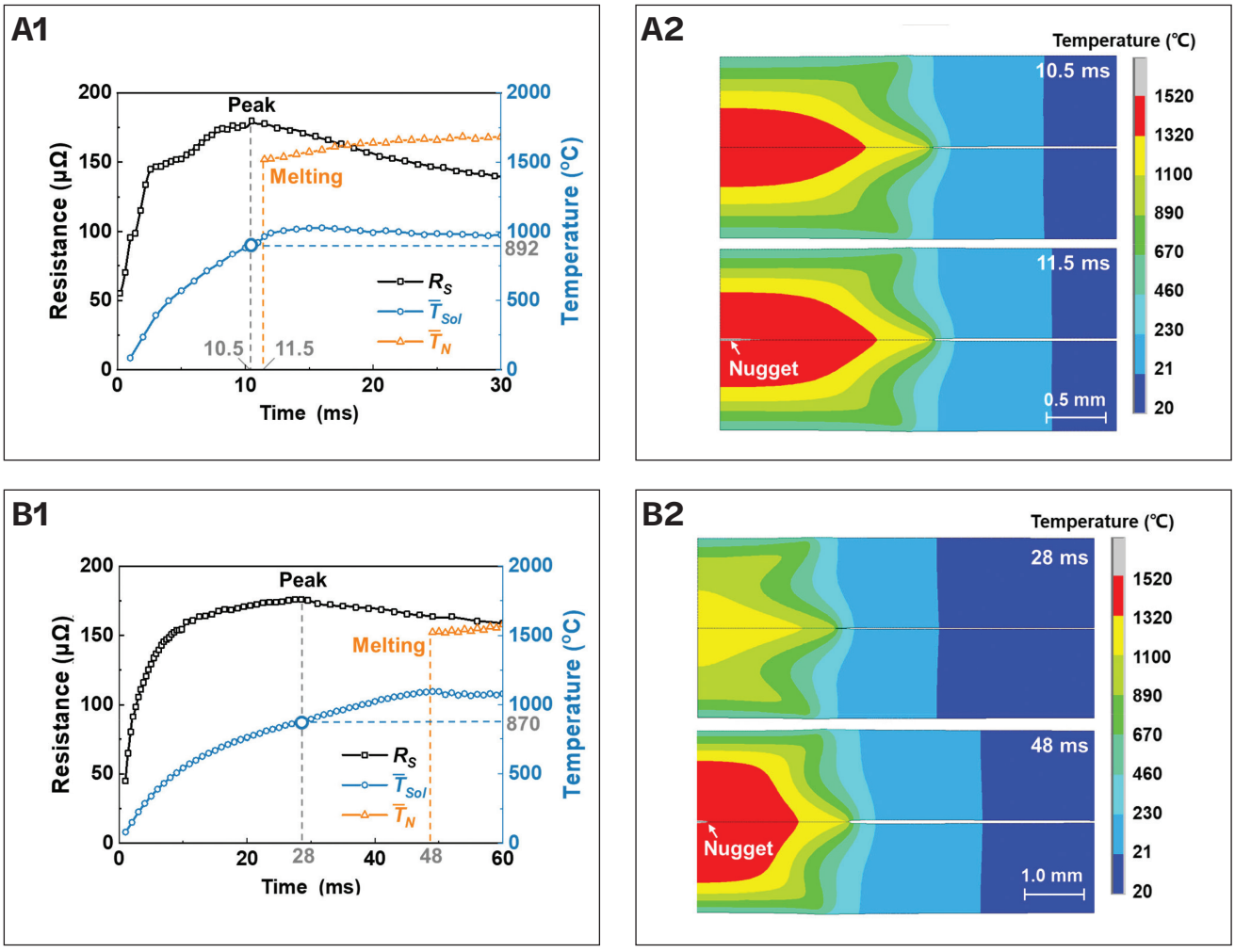

Fig. 18 — Comparative analysis between peak resistance and nugget formation for different sheet stack-ups: A1 ~ A2 — 0.8 + 0.8-mm DP590; B1 ~ B2 — 1.6 + 1.6-mm DP590.

temperature. In the temperature range of solid material, $\rho_S(T)$ is almost a convex function, and thus there exists

$$\rho_S\left(\frac{T_1+T_2}{2}\right) < \frac{\rho_S(T_1)+\rho_S(T_2)}{2} \tag{13}$$

This inequality implies that the average of resistivities associated with different temperatures is larger than the resistivity corresponding to the average of those temperatures. Accordingly, R_I, R_{II}, and R_N will be underestimated using Equation 12, leading to a smaller sheet resistance estimation. Nevertheless, $R_{EC}{}^*$ can still serve as an estimation of R_S. Combining Equations 10–12, the quantitative mapping model between the weld profile and the sheet bulk resistance can be given by

$$2R_S \approx R_{EC}{}^* = f\left(D_N, P_N, D_{\frac{E}{S}}, \bar{T}_N, \bar{T}_{Sol}\right) = \frac{4\rho_S(\bar{T}_{Sol})}{\pi + \frac{2h_S}{D_{\frac{E}{S}}} ln\left(\frac{8\pi D_{\frac{E}{S}}}{h_S} - 1\right)} \left[\frac{2h_S - P_N}{D_{E/S}^2} + \frac{\rho_S(\bar{T}_N)P_N}{\rho_S(\bar{T}_{Sol})D_N^2 + \rho_S(\bar{T}_N)\left(D_{E/S}^2 - D_N^2\right)}\right] \tag{14}$$

It was found that sheet resistance can be reconstructed through combining nugget size, electrode/sheet contact diameter, and average sheet temperature. Since this model has no unexplained pending coefficients, it shows good interpretability to reveal the intrinsic correlation mechanism between the process signal and the weld geometry.

Analysis of Resistance Drop Feature

The analytical mapping model developed enables quantitative analysis of the dynamic resistance signal's evolution mechanism. According to Equation 14, R_S can be further changed to

$$\begin{cases} 2R_S \approx \dfrac{1}{\omega_f}(R_{Sol} + \gamma\eta R_N) \\ R_{Sol} = \dfrac{4}{\pi}\rho_S(\bar{T}_{Sol})\dfrac{2h_S}{D_{E/S}^2} \end{cases} \tag{15}$$

where R_{Sol} represents the resistance of the solid material in the equivalent cylinder, and R_N stands for the resistance of the weld nugget. It can be found that R_S decomposes into

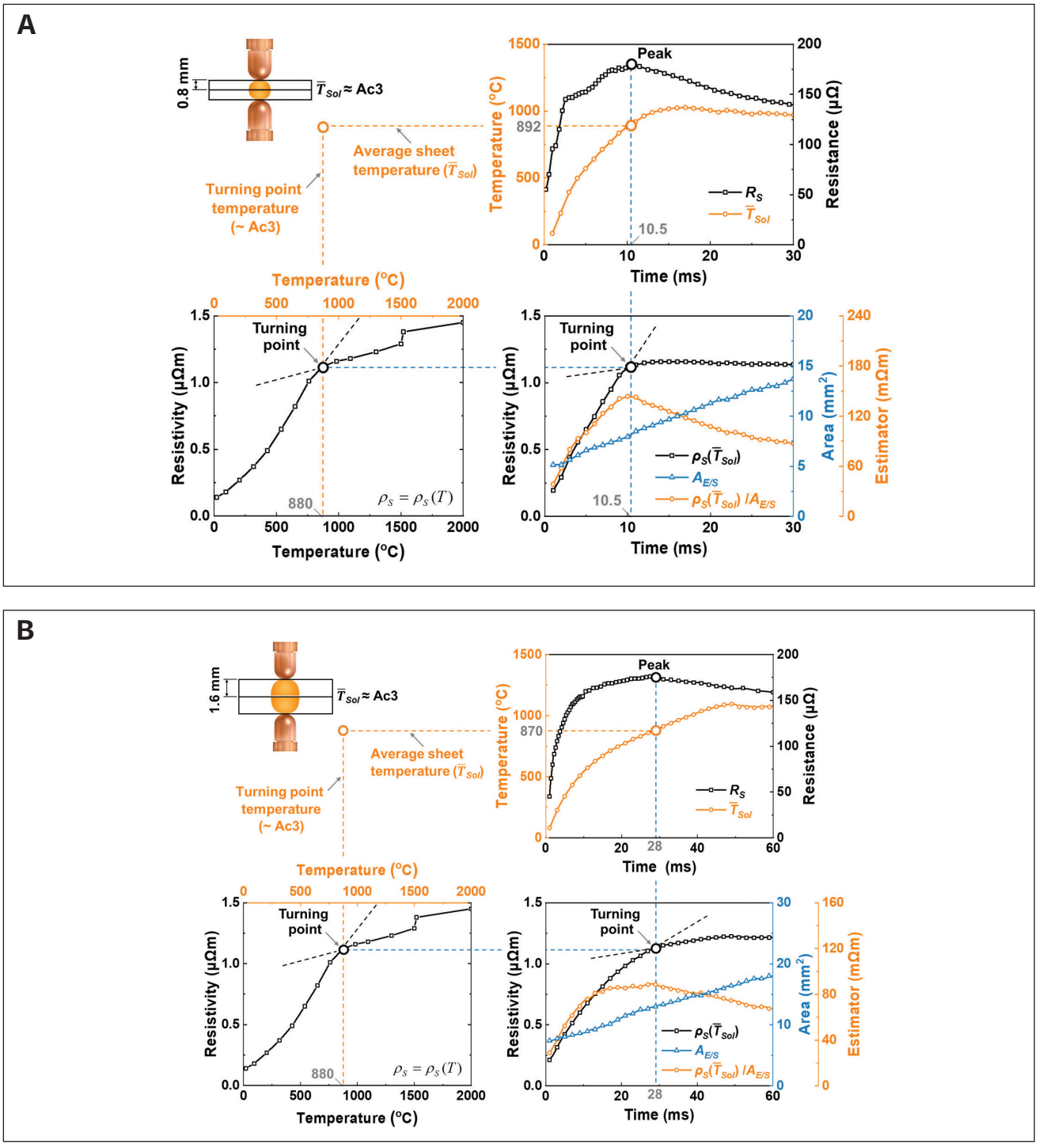

Fig. 19 — Analysis of the formation mechanism of the resistance peak feature for different sheet stack-ups: A — 0.8 + 0.8-mm DP590; B — 1.6 + 1.6-mm DP590.

two parts: an R_{Sol}-related solid component and an R_N-related molten component. In other words, R_S is reconsidered as a weighted sum of R_{Sol} and R_N, where the dimensionless weights γ and η can be given by

$$\begin{cases} \gamma^{-1} = \dfrac{1}{\left(1 - \dfrac{\rho_S(\bar{T}_{Sol})}{\rho_S(\bar{T}_N)}\right)\dfrac{D_N^2}{D_{E/S}^2}} - 1 \\ \eta = \dfrac{\rho_S(\bar{T}_{Sol})}{\rho_S(\bar{T}_N)} \cdot \dfrac{D_N^2}{D_{E/S}^2} \end{cases} \tag{16}$$

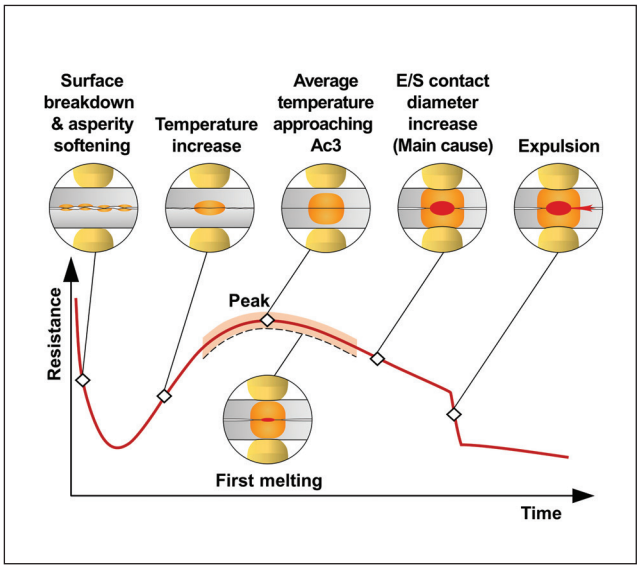

Fig. 20 — Updated evolution mechanism of the dynamic resistance signal for the bare steel RSW process.

Figures 16A and B show the evaluation of $\bar{T}_{Sol}$, $\bar{T}_N$, and the ratio of D_N and $D_{E/S}$ during the heating stage, which were obtained from the FE model. After the nugget formation (10.5 ms), $\bar{T}_{Sol}$ and $\bar{T}_N$ were near 1000° and 1650°C, respectively, so the ratio of $\rho_S(\bar{T}_{Sol})$ and $\rho_S(\bar{T}_N)$ remained almost constant. Meanwhile, after a quick increase in the first 16 ms, the ratio of D_N and $D_{E/S}$ peaked around 0.92 and stayed at a relatively steady level. Therefore, the weights γ and η can be approximated as constants, taking values of about 0.19 and 0.70, respectively. In Equation 15, the combined weight $\gamma\eta$ for R_N was approximately 0.13 while that for R_{Sol} was 1.0, indicating that $\bar{T}_{Sol}$ accounted for the majority of the sheet resistance while R_N caused less influence. This inference can also be drawn by comparing the evolution trends of solid and molten components in Fig. 16C. The solid component and R_S reached their peaks simultaneously, and the solid component's drop was primarily responsible for R_S's subsequent decline. Accordingly, the trend of the sheet resistance or even the overall dynamic resistance was mainly determined by R_{Sol} but not R_N. This implies that the evolution of the dynamic resistance signal is weakly correlated with nugget sizes such as nugget diameter and nugget thickness, contrary to the previous empirical perception.

In many previous studies (Refs. 6–9) and some commercial RSW controllers, the dynamic resistance drop (ΔR_{drop}) after its peak has been used as a key feature for evaluating nugget diameter. However, this method may not be accurate enough. Based on a Taylor series expansion of the Law of Resistance, the change of resistance (ΔR) should be proportional to the change in the diameter of the current path area (ΔD):

$$\Delta R \propto \Delta\left(\frac{1}{D^2}\right) = -2\Delta D + o(\Delta D^2) \tag{17}$$

Thus, the drop of R_S and even the overall resistance drop ΔR_{drop} should be approximately proportional to a weighted sum of the changes of $D_{E/S}$ and D_N, in accordance with Equations 7 and 15. Since R_{Sol} showed a dominant influence on R_S (see Fig. 16C), ΔR_{drop} should depend mainly on the increase of $D_{E/S}$ rather than that of D_N. A scatter chart of the experimental data for ΔR_{drop} and $D_{E/S}$ was plotted to verify this idea, as shown in Fig. 17A. A significant linear correlation between the two variables was found, so a linear regression analysis was applied to assess this correlation quantitatively. It was found that the determination coefficient R^2 exceeded 0.95. Meanwhile, a similar analysis was performed for ΔR_{drop} and D_N. The results showed a weaker correlation between them, with an R^2 of only 0.79 — Fig. 17B. This is consistent with the inference above, indicating that the resistance drop feature mainly reflects the change in the E/S contact diameter (i.e., dynamic indentation diameter) but cannot accurately describe nugget diameter growth.

Analysis of Resistance Peak Feature

According to the experimental results in Figs. 6 and 7, the first melting moment seemed to lag behind the resistance peak moment. However, the sequential relationship between the two moments was difficult to precisely determine due to the large time interval among different heating durations, especially for the 0.8 + 0.8-mm sheet stack-up. For this reason, the FE model with a time step of 0.5 ms was used to improve the time resolution. The simulated evolutions of R_S, $\bar{T}_{Sol}$, and $\bar{T}_N$ for different sheet stack-ups are shown in Fig. 18. For the 0.8 + 0.8-mm sheet stack-up, R_S peaked at 10.5 ms while melting started at 11.5 ms. For the 1.6 + 1.6-mm sheet stack-up, R_S peaked at 28 ms while melting started at 48 ms, significantly lagging behind the peak resistance moment. This indicates the viewpoint, proposed by Dickinson et al. (Ref. 11), that the first melting occurring before the peak resistance moment is not accurate enough. Meanwhile, it can also be found that $\bar{T}_{Sol}$ at the moment of resistance peak was around 880°C for both stack-ups.

Before melting occurs, D_N and P_N are equal to zero, and, thus, Equation 14 can be rewritten as

$$2R_S = \frac{2h_S}{\omega_f} \cdot \frac{\rho_S(\bar{T}_{Sol})}{A_{E/S}} \tag{18}$$

where the correction factor ω_f would gradually decrease as the E/S contact area $A_{E/S}$ increases, but its variation is relatively small. Therefore, the evolution trend of R_S is mainly determined by the ratio of $\rho_S(\bar{T}_{Sol})$ and $A_{E/S}$. Using this ratio as an estimator, it was found that the peak feature can be well reproduced, referring to the bottom right plots in Figs. 19A and B. This suggests that the peak in R_S should be attributed to the peak of the estimator. The cause of the resistance peak feature can be explained as follows: In the early stage, the average sheet temperature $\bar{T}_{Sol}$ is low, and the increase of $\bar{T}_{Sol}$ will lead to a rapid rise in $\rho_S(\bar{T}_{Sol})$. Although $A_{E/S}$ is increasing, $\rho_S(\bar{T}_{Sol})$ is growing at a much higher rate than $A_{E/S}$, making R_S a rising trend. However, there is a bilinear relationship between sheet resistivity and sheet temperature, with a turning point of around 880°C (see Table 4). When $\bar{T}_{Sol}$ approaches 880°C, $\rho_S(\bar{T}_{Sol})$ also reaches its turning point. At this moment, the growth rate of $\rho_S(\bar{T}_{Sol})$ is significantly reduced and becomes

lower than that of $A_{E/S}$, resulting in a rapid decrease in the ratio of $\rho_S(\bar{T}_{Sol})$ and $A_{E/S}$ and thus generating the peak feature in R_S. This inference applies to both stack-ups and can be considered independent of the sheet thickness, as shown in Fig. 19.

Obviously, the peak feature of the dynamic resistance signal was attributed to the bilinear relationship between sheet resistivity and sheet temperature. In other words, the root cause was the thermophysical property of the steel rather than the formation of the weld nugget. This viewpoint is consistent with the finding by Wang and Wei (Ref. 22) that the resistance peak feature will disappear when a constant resistivity is used in the numerical analysis. The turning point of sheet resistivity was related to the austenite transition, which generally occurs around the upper critical temperature Ac3 (Ref. 37). Therefore, the peak feature of the dynamic resistance signal was an indirect manifestation of the average sheet temperature reaching Ac3, while it was not related to the formation of the weld nugget.

Conclusion

This article investigates the evolution mechanism responsible for the dynamic resistance signal in the bare steel RSW process. Through collaborative simulation and analytical mapping modeling, the quantitative correlation between the resistance signal and the weld profile was interpreted, and the reasons for the formation of typical signal features were also revealed. The conclusions drawn from this study are as follows:

1) The dynamic resistance signal contains the components of sheet resistance, electrode resistance, and interface contact resistance. The sheet resistance component was the most critical component for signal reconstruction. It accounted for the largest share and determined the evolution trend of the overall dynamic resistance signal, especially when the contact resistance was eliminated after the first few milliseconds.

2) By considering the fringing effect, an analytical mapping model without any unexplained pending coefficients was developed to reveal the quantitative correlation between the sheet resistance component and the weld profile. Sheet resistance can be reconstructed through combining nugget size, electrode/sheet contact diameter, and average sheet temperature.

3) According to the mapping model, it was found that sheet resistance can be further decomposed into two parts: the solid-related base component and the nugget-related incremental component. The former occupies the major proportion and determines the evolution trend of sheet resistance, suggesting that the correlation between the dynamic resistance signal and nugget size was not that significant.

4) The resistance drop feature (i.e., the amplitude of the drop in the dynamic resistance signal after its peak) was mainly caused by the increase of electrode/sheet contact diameter. It correlates more weakly with nugget diameter than contact diameter and cannot accurately reflect the growth of nugget diameter.

5) The peak resistance feature derives from the bilinear relationship between sheet resistivity and temperature and was an indirect manifestation of the average sheet temperature approaching the upper critical temperature Ac3. However, the feature was not related to the formation of the weld nugget and does not necessarily appear after first melting.

Eventually, the evolution diagram of the dynamic resistance signal can be updated, as shown in Fig. 20. These conclusions can help correct the one-sided comprehension of dynamic resistance signal features and improve the interpretability of some data-driven methods used for RSW quality monitoring and control. Due to space limitations, this study only focuses on the RSW process of bare DP590 steel. Future research can be extended to other materials, including coated steels and aluminum alloys, to refine the evolution mechanism of the dynamic resistance signal.

Acknowledgments

The authors would like to acknowledge the financial support of the National Natural Science Foundation of China (Grant Nos. 52205396 and 52025058), the China Postdoctoral Science Foundation (Grant No. 2022T150409), the State Key Laboratory of Mechanical System and Vibration (Grant No. MSVZD202111), the State Key Laboratory of Advanced Brazing Filler Metals and Technology (Grant No. SKLABFMT202101), and the GM Research and Development Center.

References

1. Qi, L., Li, F., Zhang, Q., Xu, Y., Han, X., and Li, Y. 2021. Improvement of single-sided resistance spot welding of austenitic stainless steel using radial magnetic field. *Journal of Manufacturing Science and Engineering* 143(3): 031004. DOI: 10.1115/1.4048048

2. AWS D8.1M:2013, *Specification for Automotive Weld Quality — Resistance Spot Welding of Steel*. Miami, Fla.: American Welding Society.

3. Summerville, C., Adams, D., Compston, P., and Doolan, M. 2017. Nugget diameter in resistance spot welding: A comparison between a dynamic resistance based approach and ultrasound C-scan. *Procedia Engineering* 183: 257–263. DOI: 10.1016/j.proeng.2017.04.033

4. Zhou, K., and Yao, P. 2019. Overview of recent advances of process analysis and quality control in resistance spot welding. *Mechanical Systems and Signal Processing* 124: 170–198. DOI: 10.1016/j.ymssp.2019.01.041

5. Summerville, C., Adams, D., Compston, P., and Doolan, M. 2017. Process monitoring of resistance spot welding using the dynamic resistance signature. *Welding Journal* 96(11): 403-s to 412-s.

6. Zhao, D., Bezgans, Y., Wang, Y., Du, W., and Vdonin, N. 2021. Research on the correlation between dynamic resistance and quality estimation of resistance spot welding. *Measurement* 168(1): 108299. DOI: 10.1016/j.measurement.2020.108299

7. Xing, B. B., Xiao, Y., Qin, Q. H., and Cui, H. Z. 2017. Quality assessment of resistance spot welding process based on dynamic resistance signal and random forest based. *The International Journal of Advanced Manufacturing Technology* 94(1–4): 327–339. DOI: 10.1007/s00170-017-0889-6

8. Wan, X., Wang, Y., Zhao, D., Huang, Y., and Yin, Z. 2017. Weld quality monitoring research in small scale resistance spot welding by dynamic resistance and neural network. *Measurement* 99: 120–127. DOI: 10.1016/j.measurement.2016.12.010

9. Wan, X., Wang, Y., and Zhao, D. 2018. Quality estimation in small scale resistance spot welding of titanium alloy based on dynamic electrical signals. *ISIJ International* 58(4): 721–726. DOI: 10.2355/isijinternational.ISIJINT-2017-282

10. Jung, W., Oh, H., Yun, D. H., Kim, Y. G., Youn, J. P., and Park, J. H. 2020. Modified recurrence plot for robust condition monitoring of electrode tips in a resistance spot welding system. *Applied Sciences* 10(17): 5860. DOI: 10.3390/app10175860

11. Dickinson, D. W., Franklin, J. E., and Stanya, A. 1980. Characterization of spot welding behavior by dynamic electrical parameter monitoring. *Welding Journal* 59(6): 170-s to 176-s.

12. Kaars, J., Mayr, P., and Koppe, K. 2016. Generalized dynamic transition resistance in spot welding of aluminized 22MnB5. *Materials & Design* 106: 139–145. DOI: 10.1016/j.matdes.2016.05.097

13. Fan, Q. Y., Xu, G. C., and Gu, X. P. 2016. Expulsion characterization of stainless steel resistance spot welding based on dynamic resistance signal. *Journal of Materials Processing Technology* 236: 235–240. DOI: 10.1016/j.jmatprotec.2016.05.026

14. Luo, Y., Rui, W., Xie, X., and Zhu, Y. 2016. Study on the nugget growth in single-phase AC resistance spot welding based on the calculation of dynamic resistance. *Journal of Materials Processing Technology* 229: 492–500. DOI: 10.1016/j.jmatprotec.2015.10.006

15. Gedeon, S. A., Sorensen, C. D., Ulrich, K. T., and Eagar, T. W. 1987. Measurement of dynamic electrical and mechanical properties of resistance spot welds. *Welding Journal* 60(12): 378-s to 385-s.

16. Ighodaro, O. L.-R., Biro, E., and Zhou, Y. N. 2016. Study and applications of dynamic resistance profiles during resistance spot welding of coated hot-stamping steels. *Metallurgical and Materials Transactions A* 48(2): 745–758. DOI: 10.1007/s11661-016-3899-3

17. Batista, M., and Brandi, S. D. 2013. Use of dynamic resistance and dynamic energy to compare two resistance spot welding equipments for automotive industry in zinc coated and uncoated sheets. *American Journal of Engineering Research* 2(6): 79–93.

18. Bag, S., DiGiovanni, C., Han, X., and Zhou, N. Y. 2020. A phenomenological model of resistance spot welding on liquid metal embrittlement severity using dynamic resistance measurement. *Journal of Manufacturing Science and Engineering* 142(3): 031007. DOI: 10.1115/1.4046162

19. Simončič, S., and Podržaj, P. 2012. Image-based electrode tip displacement in resistance spot welding. *Measurement Science and Technology* 23(6): 065401. DOI: 10.1088/0957-0233/23/6/065401

20. Wei, P. S., and Wu, T. H. 2014. Effects of electrode contact condition on electrical dynamic resistance during resistance spot welding. *Science and Technology of Welding and Joining* 19(2): 173–180. DOI: 10.1179/1362171813y.0000000177

21. Cho, H. S., and Cho, Y. 1985. A theoretical model for the dynamic resistance in resistance spot welds. *Proceedings of the Institution of Mechanical Engineers, Part B: Journal of Engineering Manufacture* 199(5): 71–79. DOI: 10.1243/PIME_PROC_1985_199_050_02

22. Wang, S. C., and Wei, P. S. 2001. Modeling dynamic electrical resistance during resistance spot welding. *Journal of Heat Transfer* 123(3): 576–585. DOI: 10.1115/1.1370502

23. Zhou, K., Shi, T., and Cai, L. 2017. Online measuring the electrical resistivity of molten nugget of stainless steel in resistance spot welding. *Journal of Manufacturing Processes* 28: 109–115. DOI: 10.1016/j.jmapro.2017.05.026

24. Kas, Z., and Das, M. 2019. Adaptive control of resistance spot welding based on a dynamic resistance model. *Mathematical and Computational Applications* 24(4): 86–99. DOI: 10.3390/mca24040086

25. GMW. 2018. *Weld Acceptance Criteria and Repair Procedures Resistance Spot Welds — Steel*. GMW14057. General Motors Corp.

26. Xia, Y. J., Su, Z. W., Li, Y. B., Zhou, L., and Shen, Y. 2019. Online quantitative evaluation of expulsion in resistance spot welding. *Journal of Manufacturing Processes* 46: 34–43. DOI: 10.1016/j.jmapro.2019.08.004

27. Xia, Y. J., Su, Z. W., Lou, M., Li, Y. B., and Carlson, B. E. 2020. Online precision measurement of weld indentation in resistance spot welding using servo gun. *IEEE Transactions on Instrumentation and Measurement* 69(7): 4465–4475. DOI: 10.1109/tim.2019.2943981

28. Su, Z. W., Xia, Y. J., Shen, Y., and Li, Y. B. 2020. A novel real-time measurement method for dynamic resistance signal in medium-frequency DC resistance spot welding. *Measurement Science and Technology* 31(5): 055011. DOI: 10.1088/1361-6501/ab6673

29. Xia, Y.-J., Shen, Y., Zhou, L., and Li, Y.-B. 2021. Expulsion intensity monitoring and modeling in resistance spot welding based on electrode displacement signals. *Journal of Manufacturing Science and Engineering* 143(3): 031008. DOI: 10.1115/1.4048441

30. Qi, L., Zhang, Q., Niu, S., Chen, R., and Li, Y. 2021. Influencing mechanism of an external magnetic field on fluid flow, heat transfer and microstructure in aluminum resistance spot welding. *Engineering Applications of Computational Fluid Mechanics* 15(1): 985–1001. DOI: 10.1080/19942060.2021.1938684

31. Wan, Z., Wang, H.-P., Wang, M., Carlson, B. E., and Sigler, D. R. 2016. Numerical simulation of resistance spot welding of Al to zinc-coated steel with improved representation of contact interactions. *International Journal of Heat and Mass Transfer* 101: 749–763. DOI: 10.1016/j.ijheatmasstransfer.2016.05.023

32. Wang, J., Wang, H.-P., Lu, F., Carlson, B. E., and Sigler, D. R. 2015. Analysis of Al-steel resistance spot welding process by developing a fully coupled multi-physics simulation model. *International Journal of Heat and Mass Transfer* 89: 1061–1072. DOI: 10.1016/j.ijheatmasstransfer.2015.05.086

33. Schwenk, C., and Rethmeier, M. 2011. Material properties for welding simulation — Measurement, analysis, and exemplary data. *Welding Journal* 90(11): 220-s to 227-s.

34. Eshraghi, M., Tschopp, M. A., Asle Zaeem, M., and Felicelli, S. D. 2014. Effect of resistance spot welding parameters on weld pool properties in a DP600 dual-phase steel: A parametric study using thermomechanically-coupled finite element analysis. *Materials & Design* (1980–2015) 56: 387–397. DOI: 10.1016/j.matdes.2013.11.026

35. Song, Q. F., Zhang, W. Q., and Bay, N. 2005. An experimental study determines the electrical contact resistance in resistance welding. *Welding Journal* 84(5): 73-s to 76-s.

36. Nishiyama, H., and Nakamura, M. 1993. Capacitance of disk capacitors. *IEEE Transactions on Components, Hybrids, and Manufacturing Technology* 16(3): 360–366. DOI: 10.1109/33.232065

37. Kaars, J., Mayr, P., and Koppe, K. 2018. Determining material data for welding simulation of presshardened steel. *Metals* 8(10): 740–754. DOI: 10.3390/met8100740

YU-JUN XIA, **TIAN-LE LV**, and **YONG-BING LI** (*yongbinglee@sjtu.edu.cn*) are with the Shanghai Key Laboratory of Digital Manufacture for Thin-Walled Structures, School of Mechanical Engineering, Shanghai Jiao Tong University, Shanghai, China. **HASSAN GHASSEMI-ARMAKI** and **BLAIR E. CARLSON** are with Manufacturing Systems Research Lab, General Motors Global R&D, Warren, Mich.